JACS
JOURNAL OF THE AMERICAN CHEMICAL SOCIETY

Article

pubs.acs.org/JACS

Enhanced CO Oxidation Rates at the Interface of Mesoporous Oxides and Pt Nanoparticles

Kwangjin An,[†] Selim Alayoglu,[†] Nathan Musselwhite, Sheba Plamthottam, Gérôme Melaet, Avery E. Lindeman, and Gabor A. Somorjai*

Department of Chemistry, University of California, Berkeley, California 94720, United States

Chemical Sciences Division and Materials Sciences Division, Lawrence Berkeley National Laboratory, Berkeley, California 94720, United States

Supporting Information

ABSTRACT: The interaction of the metal and support in oxide-supported transition-metal catalysts has been proven to have extremely favorable effects on catalytic performance. Herein, mesoporous Co_3O_4, NiO, MnO_2, Fe_2O_3, and CeO_2 were synthesized and utilized in CO oxidation reactions to compare the catalytic activities before and after loading of 2.5 nm Pt nanoparticles. Turnover frequencies (TOFs) of pure mesoporous oxides were 0.0002−0.015 s^{-1}, while mesoporous silica was catalytically inactive in CO oxidation. When Pt nanoparticles were loaded onto the oxides, the TOFs of the Pt/metal oxide systems (0.1−500 s^{-1}) were orders of magnitude greater than those of the pure oxides or the silica-supported Pt nanoparticles. The catalytic activities of various Pt/oxide systems were further influenced by varying the ratio of CO and O_2 in the reactant gas feed, which provided insight into the mechanism of the observed support effect. In situ characterization using near-edge X-ray absorption fine structure (NEXAFS) and ambient-pressure X-ray photoelectron spectroscopy (APXPS) under catalytically relevant reaction conditions demonstrated a strong correlation between the oxidation state of the oxide support and the catalytic activity at the oxide−metal interface. Through catalytic activity measurements and in situ X-ray spectroscopic probes, CoO, Mn_3O_4, and CeO_2 have been identified as the active surface phases of the oxide at the interface with Pt nanoparticles.

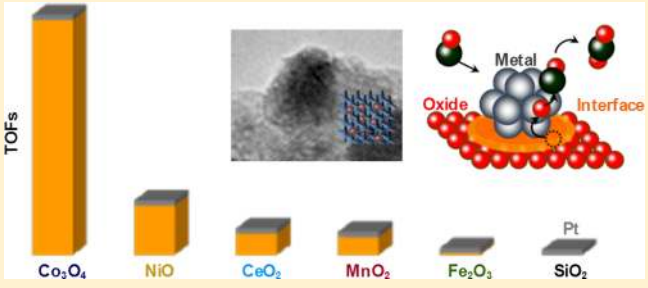

1. INTRODUCTION

The chemistry of heterogeneous catalysis on transition-metal surfaces involves the covalent bonding of neutral molecules, which leads to dissociation and rearrangements to produce other neutral atoms and molecules.[1,2] Many previous studies have demonstrated large enhancements of catalytic behavior due to the role of the oxide−metal interface, wherein charge plays a crucial role in the catalytic chemistry.[3−13] Examples include the hydrogenation of CO_2 on rhodium by many different transition-metal oxides, the use of titanium oxide as a catalyst support for CO hydrogenation (Fischer−Tropsch) reactions, and even tandem catalysis.[5−13] Despite the large amounts of research on oxide−metal interfaces, the mechanism that causes the enhanced catalytic properties is not fully understood. This is mainly due to a limitation of insight of the interfaces under catalytic reaction conditions, as opposed to pre- and postcatalysis characterizations. Through the use of synchrotron-based characterization techniques it is possible to study the surface chemistry of many catalytic systems on the molecular level in order to find vital mechanistic insights under the catalytic working conditions.[14]

Herein, numerous novel mesoporous oxides (Co_3O_4, NiO, MnO_2, Fe_2O_3, and CeO_2) were synthesized and loaded with size-controlled Pt nanoparticles to investigate the oxide−metal interface effects on catalytic CO oxidation reactions in both excess O_2 and excess CO. While pure mesoporous oxides are poor catalysts compared with pure Pt nanoparticles, all of the mesoporous oxide/Pt catalysts exhibit large enhancements of the CO oxidation rate beyond the turnover rates of pure Pt nanoparticles and pure mesoporous oxides. These systems were extensively characterized, both ex situ and in situ, in order to provide insight into the working conditions of the catalyst systems. In situ studies showed that the redox behavior of the oxides provides the charge that changes the mechanism of CO oxidation from covalent-bond chemistry to so-called acid−base or charge-transfer chemistry. This change of mechanism was found to be a general phenomenon for all of the oxide−metal interfaces studied. Through the utilization of near-edge X-ray absorption fine structure (NEXAFS) and ambient-pressure X-ray photoelectron spectroscopy (APXPS) under catalytically relevant reaction conditions, we were able to demonstrate a strong correlation between the oxidation state of the oxide support and the catalytic activity at the oxide−metal interface.

Received: August 27, 2013
Published: October 3, 2013

   dx.doi.org/10.1021/ja4088743 | J. Am. Chem. Soc. 2013, 135, 16689−16696

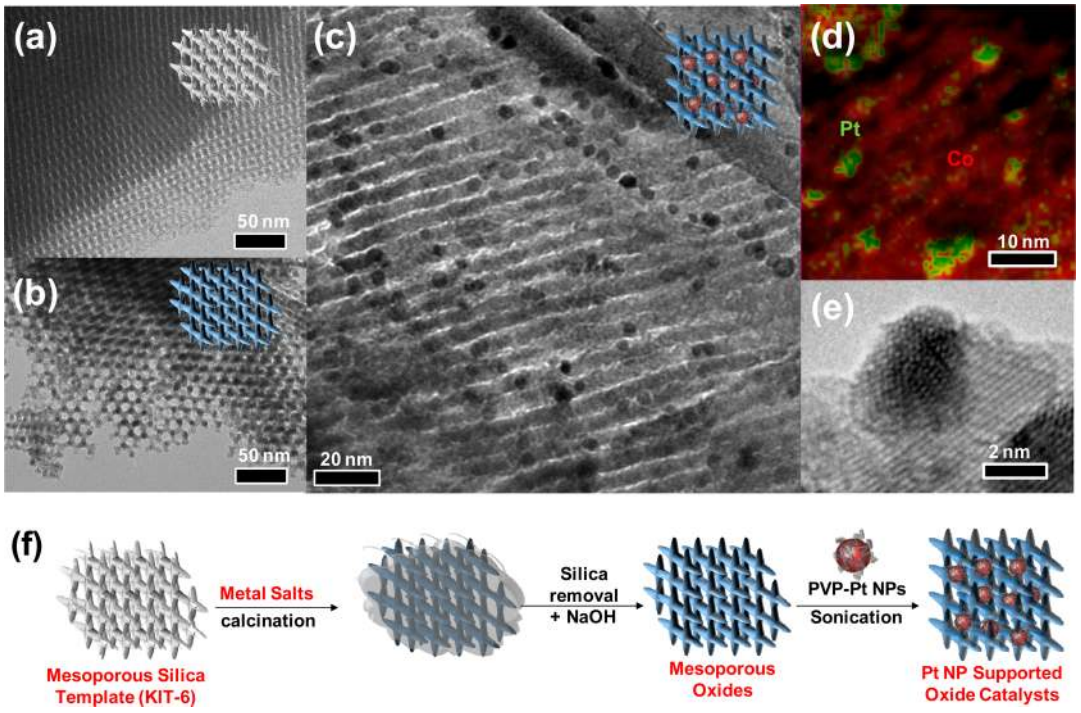

Figure 1. Preparation of Pt-nanoparticle-loaded Co_3O_4 catalysts. (a, b) TEM images of (a) the mesoporous silica template and (b) the resulting Co_3O_4 replica. (c) TEM image of Pt/Co_3O_4 catalysts and (d) their corresponding energy-dispersive spectroscopy (EDS) phase mapping, showing the merged image of the Co K (red) and Pt L (green) lines. (e) High-resolution TEM image of Pt/Co_3O_4 catalysts. (f) Illustration of the hard-templating (nanocasting) approach for the preparation of mesoporous-oxide-supported Pt nanoparticle catalysts.

2. EXPERIMENTAL SECTION

2.1. Synthesis of Mesoporous Co_3O_4, NiO, MnO_2, Fe_2O_3, and CeO_2. Mesoporous silica KIT-6 with a bicontinuous pore structure was used as a hard template.[15] For the synthesis of KIT-6, 27 g of P123 and 43.5 mL of concentrated HCl were dissolved with 980 mL of water in a polypropylene bottle, and 33.3 mL of *n*-butanol was added to the solution at 308 K with vigorous stirring. After 1 h, 58 g of TEOS was added to the solution followed by stirring at this temperature for 24 h. The capped bottle was stored at 313 K for another 24 h in an oven. The solid was filtered, dried at 363 K overnight, and calcined at 823 K for 6 h.

Mesoporous oxides were prepared through the hard-templating approach using KIT-6, which was developed by Schüth and co-workers.[16,17] $Co(NO_3)_2{\cdot}6H_2O$, $Ni(NO_3)_2{\cdot}6H_2O$, $Mn(NO_3)_2{\cdot}xH_2O$, $Fe(NO_3)_3{\cdot}9H_2O$, and $Ce(NO_3)_3{\cdot}6H_2O$ (Sigma-Aldrich) were used to synthesize mesoporous Co_3O_4, NiO, MnO_2, Fe_2O_3, and CeO_2, respectively.[16−18] In a typical synthesis, 16 mmol of metal nitrate dissolved in 8 mL of water was added to 4 g of KIT-6 in 50 mL of toluene at 338 K with stirring. After evaporation of toluene, the precipitated sol was collected and dried at 333 K overnight, followed by calcination at 573 K for 6 h. The silica template was removed completely using 2 M aqueous NaOH solution heated to 333 K followed by several washing steps with water and a final drying step at 323 K.

2.2. Preparation of Oxide-Supported Pt Nanoparticle Catalysts. Poly(vinylpyrrolidone) (PVP)-capped Pt nanoparticles with an average diameter of 2.5 nm were synthesized by following the reported methods.[19] For the preparation of oxide-supported nanoparticle catalysts, colloidal solutions of Pt nanoparticles (1 mg mL^{-1}) were diluted in ethanol. The desired amounts of solution (0.3−0.5 wt % Pt) were added to the mesoporous oxides, and the mixtures were sonicated for 3 h at room temperature using a commercial ultrasonic cleaner (Branson, 1510R-MT, 70 W, 42 kHz). The brown precipitates were separated by centrifugation (3000 rpm, 20 min), thoroughly washed with acetone and ethanol four times, and dried in an oven at 353 K overnight.

2.3. Characterization. Structural characterizations of Pt nanoparticles were performed using a Hitachi H-7650 transmission electron microscope operated at 120 kV. X-ray diffraction (XRD) patterns were measured on a Bruker D8 GADDS diffractometer using Co Kα radiation (1.79 Å). Nitrogen physisorption data were obtained on a Quantachrome Autosorb-1 analyzer. Elemental analyses by inductively coupled plasma atomic emission spectroscopy (ICP-OES) were conducted using a PerkinElmer optical emission spectrometer (Optima 7000 DV). Before an ICP-OES measurement, calibration was conducted using platinum standard (Fluka, TraceCERT, 1000 mg L^{-1}) as a certified reference material (CRM). Catalysts dissolved in aqua regia were diluted with DI water and filtered for the measurement.

2.4. Catalytic CO Oxidation. CO oxidation was performed in a laboratory-scale flow reactor operated at atmospheric pressure over the temperature range between 373 and 573 K. Gas flows (Praxair, UHP) were regulated using calibrated mass-flow controllers. Temperature was controlled using a type-K thermocouple and a PID controller (Watlow 96). Catalyst (0.01−0.1 g) was diluted with low-surface-area quartz sand (washed with acid, rinsed with DI water, and calcined before use) and loaded into quartz reactors. Two different CO oxidation rates were acquired, in 100 Torr CO and 40 Torr O_2 with a balance of He for net reducing conditions or in 40 Torr CO and 100 Torr O_2 with a balance of He for net oxidizing conditions. Gas compositions were analyzed with a thermal conductivity detector (TCD) on an HP 5890 Series II gas chromatograph (GC). For comparison, mesoporous silica SBA-15 was used with and without loading of Pt nanoparticles for this reaction.[19] When the SBA-15 was used solely for CO oxidation, no activity was obtained up to a temperature of 673 K. Turnover frequencies (TOFs) were calculated by normalizing the conversion to the number of available surface Pt atoms as measured by ethylene hydrogenation and calculated on the basis of size arguments. Ethylene hydrogenation activities were used to determine the number of Pt surface sites per unit mass of catalyst by using the known TOF of 11 molecules of ethylene per surface Pt per second at 293 K with 100 Torr H_2 and 10 Torr C_2H_4.[20] The TOF values of the mesoporous oxides were determined by taking the

dx.doi.org/10.1021/ja4088743 | J. Am. Chem. Soc. 2013, 135, 16689−16696

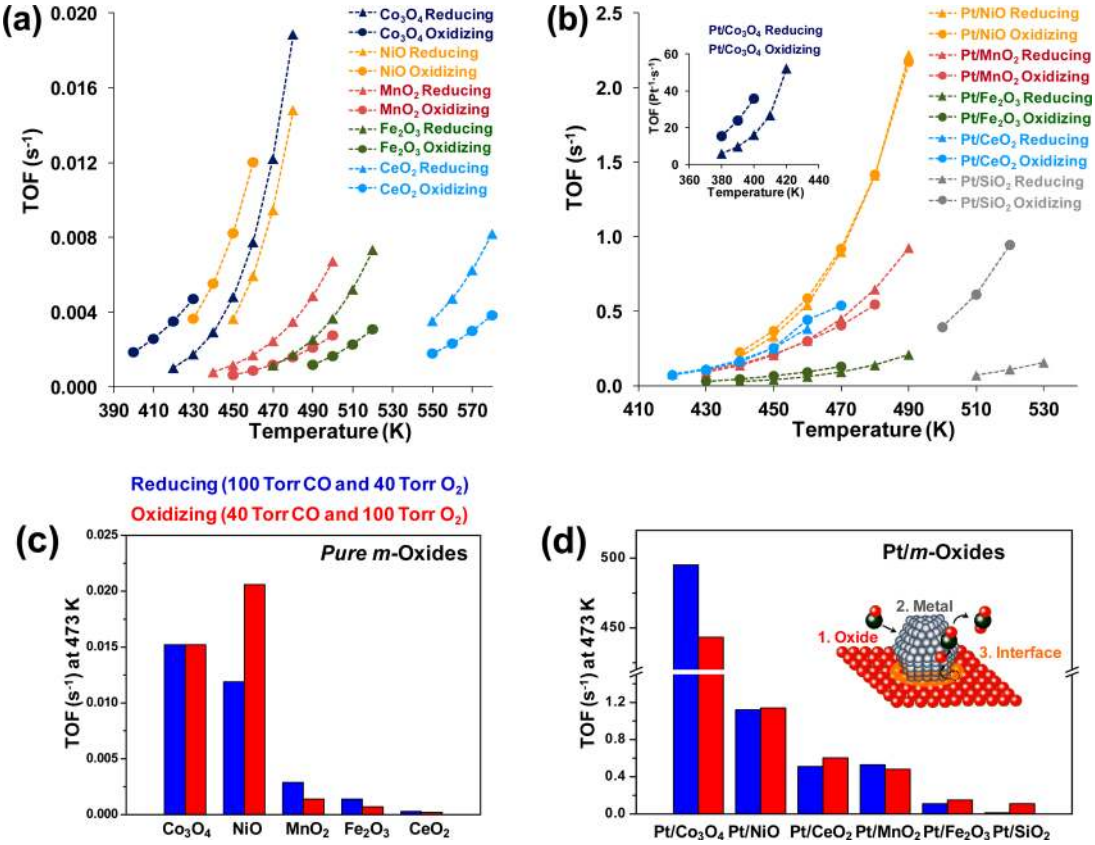

Figure 2. CO oxidation over (a, c) pure mesoporous oxides and (b, d) Pt-nanoparticle-loaded oxide catalysts. (a, b) Temperature-dependent turnover frequencies (TOFs) under either net reducing (100 Torr CO and 40 Torr O_2 with a balance of He) or net oxidizing (40 Torr CO and 100 Torr O_2 with a balance of He) conditions. (c, d) Comparison of TOFs at 473 K. The inset in (d) is an illustration showing the potential reaction sites of Pt-nanoparticle-loaded oxide catalysts during CO oxidation.

molecular production rates measured per unit surface site of the oxides based on their BET surface areas (m^2 g^{-1}) and crystalline structures. The TOFs of the Pt−oxide interfaces (i.e., after subtraction of the contributions from pure Pt and metal oxide) were calculated from the number of surface Pt sites.

2.5. In Situ Characterizations. APXPS and NEXAFS experiments were performed at beamlines 9.3.2 and 7.0.1 of the Advanced Light Source (ALS) at Lawrence Berkeley National Laboratory. NEXAFS studies were carried out in our purpose-built flow cell. Supported catalysts were exposed to pure CO or O_2 or a CO/O_2 mixture (either 39 Torr O_2 and 15 Torr CO or 39 Torr CO and 15 Torr O_2) at 473 or 523 K. The NEXAFS total electron yield (TEY) spectra with 0.3 eV resolution at the metal L (Co and Mn) or M (Ce) edge were monitored via a current amplifier by detecting compensating electrons from ground to the sample.[21] The oxidation states of the metal oxides in the near-surface regions were determined by a linear-combination fitting of the reference compounds.[21]

APXPS at beamline 9.3.2 of the ALS was conducted because it overcomes the limitations of short mean free paths of emitted photoelectrons by bringing a small aperture cone, which is differentially pumped, very close to the sample surface, which is in the reaction gas mixture.[22]

3. RESULTS AND DISCUSSION

3.1. Preparation of Mesoporous Oxides of Co_3O_4, β-MnO_2, NiO, α-Fe_2O_3, and CeO_2 and Pt-Loaded Oxide Catalysts. Mesoporous Co_3O_4, NiO, MnO_2, Fe_2O_3, and CeO_2 were prepared through the hard-templating (nanocasting) approach using mesoporous silica templates.[16−18] The hard template determines the final structure of the oxide and provides stability during high-temperature crystallization.[17,23,24] In the present study, KIT-6 mesoporous silica was used as a hard template with an ordered bicontinuous mesostructure with cubic *Ia*3*d* symmetry.[15] When metal nitrates as metal oxide precursors were combined with KIT-6 in solution, they were completely impregnated into the silica templates and readily converted to the desired crystalline oxides after calcination at 573 K. The KIT-6 was removed completely by washing with aqueous NaOH solution, leaving mesoporous Co_3O_4, β-MnO_2, NiO, α-Fe_2O_3, and CeO_2 replicas. Figure 1 shows a general nanocasting approach for the preparation of ordered mesoporous oxides and representative transmission electron microscopy (TEM) images of the KIT-6 silica template, mesoporous Co_3O_4, and Pt-nanoparticle-loaded Co_3O_4 catalysts. TEM images of the mesoporous oxides demonstrated that the well-ordered structures and the wall thicknesses (ca. 3 nm) of the oxides were in accordance with the replicated KIT-6 (see Figures S1−S3 and Table S1 in the Supporting Information).

PVP-capped Pt nanoparticles with an average diameter of 2.5 nm were incorporated into the mesoporous oxides for the preparation of Pt nanoparticle-loaded mesoporous oxide catalysts. Sonication induced efficient dispersion of the Pt nanoparticles over the inner pores of the mesoporous oxides.[19] The TEM image in Figure 1c clearly shows that the Pt nanoparticles were deposited and well-dispersed on mesoporous Co_3O_4 homogenously. Elemental analyses by energy-dispersive spectroscopy (EDS) phase mappings on Pt/Co_3O_4 (Figure 1d) were in agreement with the values obtained by ICP-OES (i.e., 0.38 wt % Pt).

dx.doi.org/10.1021/ja4088743 | J. Am. Chem. Soc. 2013, 135, 16689−16696

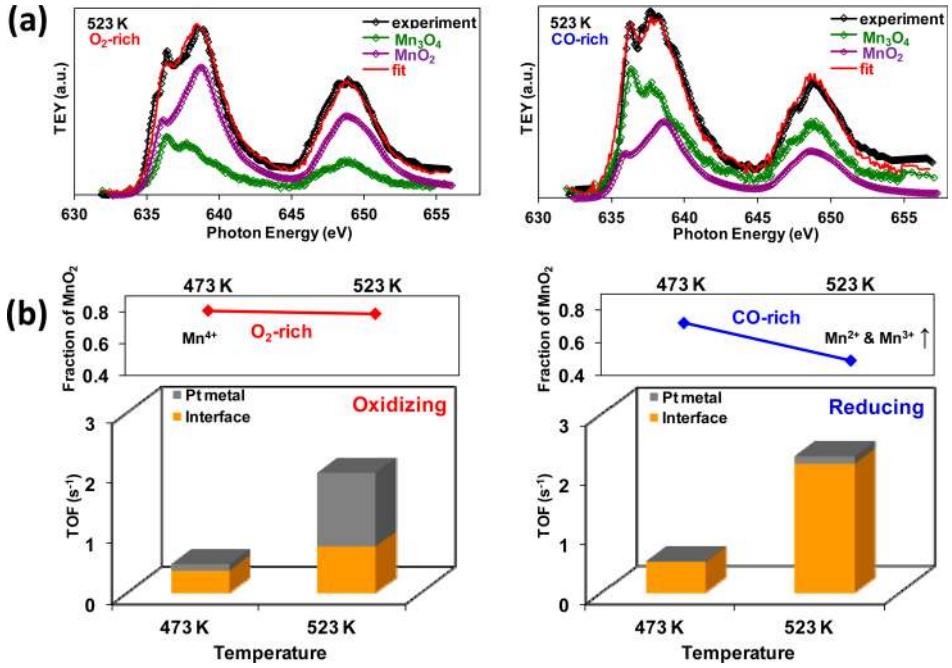

Figure 3. (a) Near-edge X-ray absorption fine structure (NEXAFS) total electron yield (TEY) spectra at the Mn L edges for the Pt/MnO_2 catalyst and (b) graphs correlating the catalytic activity (TOF) and oxidation state of Mn in CO oxidation. Shown in (a) are representative linear-combination fittings obtained at 523 K under (left) 15 Torr CO and 39 Torr O_2 (O_2-rich) and (right) 39 Torr CO and 15 Torr O_2 (CO-rich) conditions. The top panels in (b) show the proportions of MnO_2 obtained by linear-combination fitting of the reference compounds to the NEXAFS spectra, and the corresponding TOF plots at both 473 and 523 K under different reaction conditions are given in the bottom panels. The bar graphs showing the total TOFs of the Pt/MnO_2 catalyst have been decomposed into the contributions of pure Pt (in gray) and the $Pt-MnO_2$ interface (in orange). The TOFs exhibited by pure mesoporous MnO_2 were too small to be represented.

3.2. CO Oxidation on Pure Mesoporous Oxides. Mesoporous oxides have shown notable catalytic activity as heterogeneous catalysts even in the absence of noble metals.[16,25−31] Ren et al.[18] studied ordered mesoporous oxides of Co_3O_4, Cr_2O_3, CuO, Fe_2O_3, MnO_2, Mn_2O_3, NiO, and CeO_2 as catalysts for CO oxidation. In their study, Co_3O_4, β-MnO_2, and NiO exhibited high CO oxidation activities, which were determined by measuring the temperatures required for 50% CO conversion (T_{50}). In order to study the catalytic activity of the metal−support interaction and the effect of gas feed composition, CO oxidation was carried out under two different sets of conditions, with either reducing (100 Torr CO and 40 Torr O_2 with a balance of He) or oxidizing (40 Torr CO and 100 Torr O_2 with a balance of He) gas feeds. The reaction was performed in a laboratory-scale flow reactor operated at atmospheric pressure over the temperature range between 373 and 573 K. It has been reported that Co_3O_4 shows extraordinarily high low-temperature activity, and Co^{3+} is believed to be an active site in CO oxidation.[29−31] Jansson et al.[29] proposed that CO oxidation over Co_3O_4 proceeds through a redox cycle in which gas-phase CO adsorbs on a cobalt site and subsequently reacts with a lattice oxygen atom. This then forms CO_2(g) and an oxygen vacancy, thus reducing the oxidation state of the cobalt site to Co^{2+}. Reoxidation of the cobalt site occurs with gas-phase oxygen.

As shown in Figure 2a, pure Co_3O_4 and NiO showed higher TOFs (normalized to surface area) than MnO_2, Fe_2O_3, and CeO_2 under both reducing and oxidizing conditions. The TOFs of MnO_2, Fe_2O_3, and CeO_2 under the net reducing reaction conditions were much higher than those under the net oxidizing reaction conditions. On the contrary, the catalytic activity of NiO was found to be higher under O_2-rich conditions than under CO-rich conditions. Intrinsic properties of the oxides seem to determine the catalytic behavior under these oxidizing or reducing reaction conditions.

3.3. CO Oxidation Studies on a Pt-Nanoparticle-Loaded Silica Support. In order to find the contribution to the catalytic activity of only Pt nanoparticles, mesoporous silica was used as an inert support. It has been shown that mesoporous silica, such as SBA-15 or MCF-17, does not contribute to the catalytic activity of Pt for many reactions.[18] When pure SBA-15 was solely used for CO oxidation in the current study, no conversion was found up to 673 K. In Figure 2a, the TOF for the Pt/SiO_2 catalyst was substantially higher under the O_2-rich reaction conditions than under the CO-rich reaction conditions across the temperature range studied. The TOFs for CO oxidation over Pt/SiO_2 were 0.014 and 0.11 s^{-1} at 473 K under CO- and O_2-rich reaction conditions, respectively. Goodman and co-workers[32] reported TOF values of 0.01−0.1 s^{-1} at 473 K and an activation energy of ca. 26 kcal/mol over Pt/SiO_2 catalysts and Pt(100) single crystals under CO-rich reaction conditions, which are in agreement with the values for the Pt/SiO_2 catalyst from this work (0.014−0.11 s^{-1} and 23 kcal/mol).

CO oxidation on Pt-group metal surfaces has been shown to be structure-insensitive under CO-dominant conditions, under which the reaction rate is limited by CO adsorption because CO blocks the active sites for O_2 adsorption and dissociation.[32−35] This agrees with our findings on CO oxidation over Pt nanoparticles supported on SiO_2, which exhibited no size dependence of the TOFs over the size range from 1.5 to 5 nm under both CO- and O_2-rich reaction conditions.

3.4. CO Oxidation Studies of Pt-Nanoparticle-Loaded Mesoporous Oxide Systems. When Pt nanoparticles were

dx.doi.org/10.1021/ja4088743 | J. Am. Chem. Soc. 2013, 135, 16689−16696

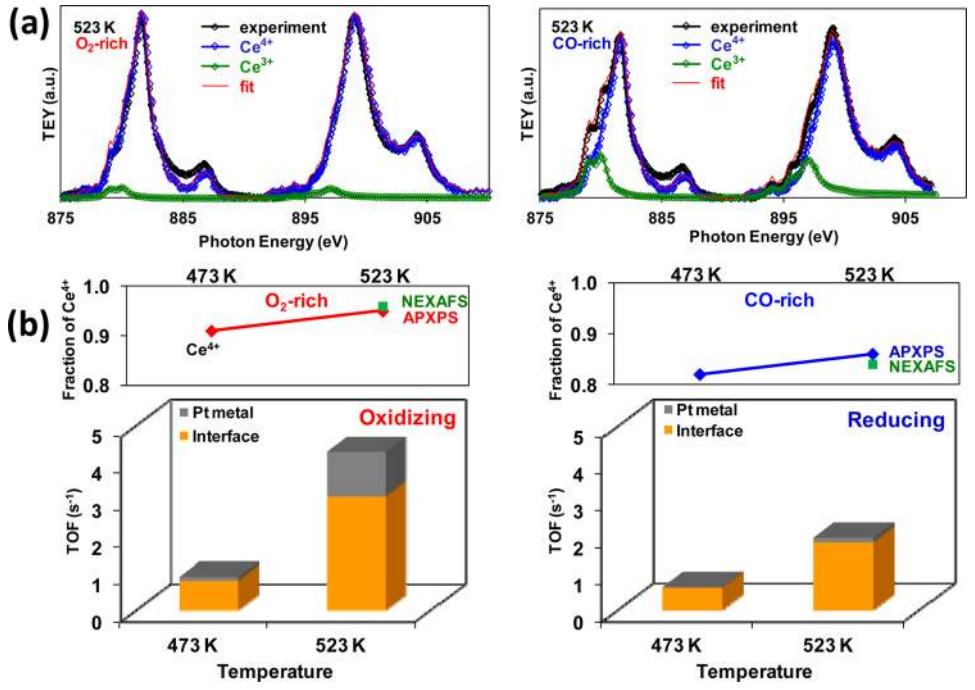

Figure 4. (a) NEXAFS TEY spectra at the Ce M edges for the Pt/CeO_2 catalyst and (b) graphs correlating the catalytic activity (TOF) and oxidation state of Ce in CO oxidation. Shown in (a) are representative linear-combination fittings obtained at 523 K under (left) 15 Torr CO and 39 Torr O_2 (O_2-rich) and (right) 39 Torr CO and 15 Torr O_2 (CO-rich) conditions. The top panels in (b) show the proportions of Ce^{4+} obtained by linear-combination fitting of the reference compounds to the NEXAFS spectra and analysis of Ce 4d XPS spectra, and the corresponding TOF plots at both 473 and 523 K under different reaction conditions are given in the bottom panels. The bar graphs showing the total TOFs of the Pt/CeO_2 catalyst have been decomposed into the contributions of pure Pt (in gray) and the $Pt–CeO_2$ interface (in orange). The contribution of pure mesoporous CeO_2 was too small to be represented. It should be noted that both the line plots and bar graphs are given to the same scale.

loaded into the mesoporous oxides, the observed catalytic TOFs were significantly higher than those expected simply by summing the contributions from the oxide support and the pure Pt nanoparticles. This enhancement can be attributed to activity at the oxide–metal interface coupled with the activities of the oxide and Pt (Figure 2b). The TOFs over the Pt-loaded oxide catalysts were 495.27, 1.12, 0.57, 0.53, and 0.11 Pt^{-1} s^{-1} at 473 K under CO-rich reaction conditions and 443.31, 1.14, 0.60, 0.48, and 0.15 Pt^{-1} s^{-1} at 473 K under O_2-rich reaction conditions for Pt/Co_3O_4, Pt/NiO, Pt/CeO_2, Pt/MnO_2, and Pt/Fe_3O_4, respectively. The contributions of the oxide–metal interfaces were found to be orders of magnitude greater than those of Pt and the oxides regardless of the gas composition (Figure 2c,d). When Pt nanoparticles were loaded on the mesoporous oxides, the reaction rates were further altered by the redox behaviors of the oxide supports. Since the 3d-block metal oxides are subject to alternation of their oxidation states under redox gas atmospheres, synergistic acid–base and/or redox sites are regarded as the key for the catalytic oxidation reaction.[36−38] The fact that the TOFs over the Pt/NiO, Pt/MnO_2, Pt/Fe_2O_3, and Pt/CeO_2 catalysts were identical under the net reducing and net oxidizing reaction atmospheres strongly suggests the existence of a catalytic reaction pathway at the interface between the CO-covered Pt and metal oxide surfaces. We observed that the Pt/SiO_2 catalyst showed less activity in the CO-rich environment than under the O_2-rich reaction conditions. This is in line with the CO/O_2 reaction rate being inversely proportional to the CO partial pressure over the Pt catalyst because of the surface poisoning effect of CO.[39,40] The extraordinarily large enhancements of the reaction rates over the Pt-loaded oxide catalysts and the changes in their TOFs under the net reducing reaction conditions can be explained by the following pathway:[10,41,42] (1) chemisorption of CO on the Pt surface; (2) migration of the CO adsorbate to the interface between Pt and the oxide; (3) formation of active oxygen in the oxide lattice of the metal interface; (4) reaction between the chemisorbed CO and the activated oxygen at the interface; and (5) refill of oxygen vacancies in the oxide by gaseous O_2.

3.5. In Situ Characterization of Oxide Catalysts during CO Oxidation. In order to understand the observed behaviors of activity enhancement, in situ characterizations using NEXAFS and APXPS were conducted under catalytically relevant reaction conditions.[43] Briefly, supported Pt/Co_3O_4, Pt/MnO_2, and Pt/CeO_2 catalysts were exposed to pure CO or O_2 or a CO/O_2 mixture [−39 Torr O_2 and 15 Torr CO (denoted as O_2-rich) or 39 Torr CO and 15 Torr O_2 (denoted as CO-rich)] at 473 or 523 K. Figure 3a shows NEXAFS TEY spectra of the Pt/MnO_2 catalyst at 523 K under the O_2-rich and CO-rich reaction conditions. A linear-combination fitting of the reference compounds indicated that an excess of the MnO_2 phase (a fraction of 0.8) was present in equilibrium with the spinel Mn_3O_4 phase under the O_2-rich conditions. Under the CO-rich reaction conditions, however, the surface regions were further reduced, resulting in a 50:50 mixture of the MnO_2 and Mn_3O_4 phases (Figure 3). Figure 3b shows the proportions of MnO_2 on the surface and TOFs that have been decomposed into metal–oxide interface and Pt metal contributions during the CO/O_2 reactions at 473 and 523 K. We found a strong correlation between the oxidation state of Mn and the normalized catalytic activity at the metal–oxide interface. In the O_2-rich reaction, the fraction of MnO_2 was changed very

dx.doi.org/10.1021/ja4088743 | J. Am. Chem. Soc. 2013, 135, 16689−16696

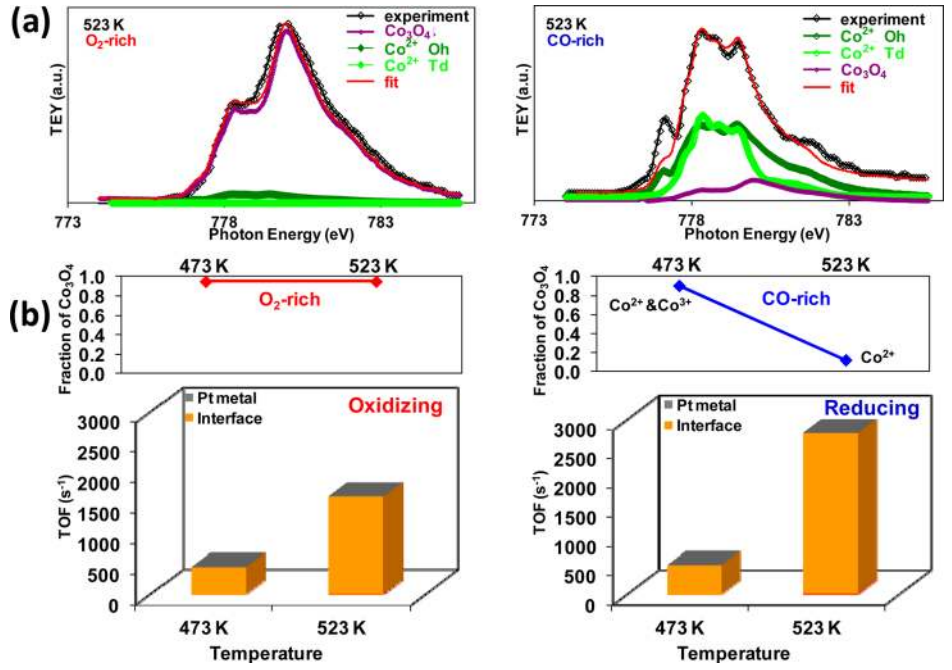

Figure 5. (a) NEXAFS TEY spectra at the Co L edges for the Pt/Co_3O_4 catalyst and (b) graphs correlating the catalytic activity (TOF) and oxidation state of Co in CO oxidation. Shown in (a) are representative linear-combination fittings obtained at 523 K under (left) 15 Torr CO and 39 Torr O_2 (O_2-rich) and (right) 39 Torr CO and 15 Torr O_2 (CO-rich) conditions. The top panels in (b) show the proportions of Co_3O_4 obtained by linear-combination fitting of the reference compounds to the NEXAFS spectra, and the corresponding TOF plots at both 473 and 523 K under different reaction conditions are given in the bottom panels. The bar graphs showing the total TOFs of the Pt/Co_3O_4 catalyst have been decomposed into the contributions of pure Pt (in gray) and the $Pt-Co_3O_4$ interface (in orange). The contribution of pure mesoporous Co_3O_4 was too small to be represented.

little (from 0.81 at 473 K to 0.79 at 523 K). In parallel with this, the turnover rate at the metal−oxide interface (color-coded in orange) was slightly increased from 0.37 to 0.77 s^{-1}, exhibiting a marginal change in CO oxidation rate at the interface compared with pure Pt (color-coded in gray) (Figure 3b, left). However, in the CO-rich reaction, both the extent of the reduction of Mn and the relative change in turnover rates at the metal−oxide interface were substantial. The fraction of MnO_2 phase decreased from 0.72 to 0.49, while the turnover rate at the interface jumped from 0.51 to 2.16 s^{-1}, which was an order of magnitude change with respect to pure Pt. On the basis of the observed trend, spinel Mn_3O_4 was identified as the dominant phase at the metal−support interface and thus the species responsible for the orders of magnitude enhancement in the CO oxidation rate.

Both a bifunctional mechanism[44] and a Mars−van Kravelen mechanism[36−38] could potentially explain the catalytic activity enhancement by the support in this case; however, neither could give insight into the detailed reaction scheme of the CO-rich or CO-deficit atmospheres. The O 1s APXPS spectra of the Pt/MnO_2 catalyst were obtained under CO-rich and O_2-rich CO/O_2 reaction conditions at 473 K. In these spectra, the peak at 529 eV was assigned to the lattice oxygen of MnO_2[45,46] and the higher-binding-energy peak at 531 eV is due to OH species or adsorbed H_2O[46] (Figure S8 in the Supporting Information). The normalized XPS intensities indicate that the lattice oxygen was more abundant under the O_2-rich reaction conditions than under the CO-rich conditions, although the CO/O_2 reaction was more favorable under the CO-rich conditions. From these results, we concluded that the interfacial reaction is governed by the oxidation state of MnO_2.

This phenomenon was not limited to the case of the Pt/MnO_2 catalyst but could be generalized to the other Pt/metal oxide systems. The Pt/CeO_2 catalyst exhibited greater overall interfacial enhancement under the O_2-rich conditions, while it was more dramatic relative to pure Pt under the CO-rich reaction condition. APXPS and NEXAFS independently revealed that the near-surface region (ca. 2 nm) of the Pt/CeO_2 catalyst mainly was composed of Ce^{4+} during the CO/O_2 reaction at 523 K. On the other hand, the Ce^{3+} concentration was appreciable (ca. 15%) under CO-rich conditions but was negligibly small (less than 5%) under O_2-rich conditions at 523 K, suggesting that CO reduces CeO_2 without apparent reaction turnovers (Figure 4). The O 1s APXPS spectra also indicated no correlation between lattice oxygen (or OH) and the reaction rate (Figure S9 in the Supporting Information). The overlapping conclusion was that Ce^{4+} sites give rise to the interfacial enhancement over the Pt/CeO_2 catalyst during the CO/O_2 reaction: Ce^{3+} sites formed upon reduction of CeO_2 under the CO-rich conditions, rendering the overall enhancement (i.e., higher turnover rates under O_2-rich vs CO-rich conditions) without significantly impacting the enhancement factor (i.e., similar orders of magnitude enhancement at the interface relative to pure Pt).

For the Pt/Co_3O_4 catalyst, the characteristic NEXAFS spectra of spinel Co_3O_4 at the Co L edge were mainly maintained under CO-rich reaction conditions at and below 473 K, whereas CoO formed as the dominant phase at the expense of the spinel Co_3O_4 phase above 523 K under the CO-rich conditions (Figure 5). Our linear-combination fitting indicated the simultaneous formation of two CoO phases: one with Co(II) in octahedral sites and another with Co(II) in tetrahedral sites.[20] For the reaction in the O_2-rich environment,

dx.doi.org/10.1021/ja4088743 | J. Am. Chem. Soc. 2013, 135, 16689−16696

the spinel Co_3O_4 phase remained dominant over the whole temperature range studied, in agreement with the findings of Oku and Sato.[47] From the viewpoint of catalysis, the CO oxidation rates were enhanced by 4 orders of magnitude at the metal−oxide interface under both the CO- and O_2-rich conditions; however, the enhancement factor was greater in the case of the CO-rich reactions, where CoO phases were dominant at the near-surface regions (Figure 5). While Co(III) sites were usually attributed to the CO/O_2 reaction turnovers on pure Co_3O_4,[48] we found that Co(II) sites are responsible for the orders of magnitude enhancement in the reaction kinetics at the metal−oxide interface.

Through catalytic activity measurements and in situ surface probe experiments, we identified that Mn^{2+} and Mn^{3+} in spinel Mn_3O_4, Ce^{4+} in CeO_2, and Co^{2+} in Co_3O_4 are the active surface phases of the oxides in contact with Pt nanoparticles. The mesoporous oxides of 3d transition metals (Co and Mn) appeared to be more active in CO oxidation at a reduced form of the oxide in contact with Pt, while CeO_2 exhibited the opposite behavior, as Ce^{4+} was catalytically more active than Ce^{3+} when interfaced with Pt. This reflects on the fact that the catalytic TOF on the Pt/CeO_2 catalyst under the O_2-rich reaction conditions was significantly larger than that under the CO-rich reaction conditions.

On the basis of our measurements of oxidation state and catalytic activities, we propose the existence of a charge-flow channel for the catalytic oxidation of CO. The role of Pt is to provide metal sites for charge to flow at Schottky interfaces, which in return create a new reaction pathway for CO to be oxidized at such high rates.[49−52] This explanation is based on previous studies that measured the flow of hot electrons simultaneously with turnover rates for the CO/O_2 and H_2/O_2 reactions using catalytic nanodiodes constructed from ca. 4 nm thick Pt films deposited on titanium oxide to form Schottky barriers.[49] The current flow across the rectifying barrier was linearly correlated with the reaction turnover rate, indicating the major role of electron flow at the $Pt−TiO_2$ interface in the catalytic reactions. However, the turnover rates were 10^4 times greater than the electron flow rates measured at steady state, indicating that the electrons have several competing reaction paths (such as absorption at defect sites, heating by the thermoelectric effect, etc.) in addition to becoming part of the transition state (such as CO_2^- or H_2O^-) that controls their influence on the catalytic reaction.[52] We believe that cobalt oxide has a higher concentration of electrons choosing the reaction path that enhances the catalytic turnover for some reason that is yet to be determined. It should be mentioned that cobalt oxide is an active material in studies of water splitting using solar energy, probably for similar reasons of efficient charge transfer during the chemical process.

4. CONCLUSIONS

At the interfaces of Pt nanoparticles and mesoporous oxides, we have observed great enhancements of catalytic activity in CO oxidation, which has rendered the "structure-insensitive" reaction on pure Pt surfaces very much "structure-sensitive" at oxide metal interfaces. Compared with pure Pt nanoparticles and pure mesoporous oxides, the turnover rates were increased by orders of magnitude with catalysis by the Pt−oxide interface. The reaction rates over Pt-nanoparticle-loaded oxide catalysts were further controlled by the redox properties of the oxides at the oxide−metal interface under reducing reaction conditions. Even under O_2-deficient reaction conditions, active oxygen could be provided from the oxide lattice. The redox chemistry in the near-surface regions of the oxide catalysts was dynamic, depending on the temperature and whether CO- or O_2-rich atmospheres were utilized during the reaction. It appears that the redox behaviors of the oxides provide the charges that participate at the oxide−metal interface, which act to amplify the CO oxidation. Through in situ characterizations using NEXAFS and APXPS under alternating redox conditions combined with catalytic activity measurements, we found that CoO, Mn_3O_4, and CeO_2 are responsible for the orders of magnitude enhancement in CO oxidation rate as the active surface phases of the oxide at the interface with Pt nanoparticles. This discovery of the relationship between surface redox chemistry and catalytic activity offers great advancements in the knowledge of how the oxide−metal interface functions during catalytic reactions. The in-depth understanding of these phenomena will have wide implications in understanding catalytic selectivity on charged and polar oxide surfaces for a number of heterogeneous transformations.

■ ASSOCIATED CONTENT

Supporting Information

TEM, XRD, and nitrogen adsorption−desorption isotherms of mesoporous oxides (Figures S1−S3 and Table S1); Pt size distribution histograms of the supported catalysts (Figures S4 and S5); conversions, Arrhenius plots, TOFs, and activation energies for CO oxidation (Figures S6 and S7 and Table S2); and APXPS spectra of Pt/oxide catalysts (Figures S8 and S9). This material is available free of charge via the Internet at http://pubs.acs.org.

■ AUTHOR INFORMATION

Corresponding Author

somorjai@berkeley.edu

Author Contributions

†K.A. and S.A. contributed equally.

Notes

The authors declare no competing financial interest.

■ ACKNOWLEDGMENTS

This work was supported the Director, Office of Basic Energy Sciences, Materials Sciences and Engineering Division, U.S. Department of Energy, under Contract DE-AC02-05CH11231. The user project at the Advanced Light Source and the Molecular Foundry at the Lawrence Berkeley National Laboratory was supported by the Director, Office of Science, Office of Basic Energy Sciences, U.S. Department of Energy, under Contract DE-AC02-05CH11231. The nanoparticle synthesis was funded by Chevron Corporation. We thank Professors A. Paul Alivisatos and Peidong Yang for use of the TEM and XRD instruments and Dr. Harun Tüysüz and Dr. Jungwon Park for valuable discussions.

■ REFERENCES

(1) Geus, J. W., van Ween, J. A. R. In *Catalysis: An Integrated Approach to Homogeneous, Heterogeneous and Industrial Catalysis*; Moulijn, J. A., van Leeuwen, P. W. N. M., van Santen, R. A., Eds.; Elsevier: Amsterdam, 1993.

(2) Somorjai, G. A. *Introduction to Surface Chemistry and Catalysis*; Wiley: New York, 1994.

(3) Schwab, G. M.; Koller, K. *J. Am. Chem. Soc.* **1968**, *90*, 3078.

(4) Somorjai, G. A.; Park, J. Y. *Angew. Chem., Int. Ed.* **2008**, *47*, 9212.

(5) Boffa, A. B.; Lin, C.; Bell, A. T.; Somorjai, G. A. *Catal. Lett.* **1994**, *27*, 243.
(6) Tauster, S. J.; Fung, S. C.; Garten, R. L. *J. Am. Chem. Soc.* **1978**, *100*, 170.
(7) Wang, S. Y.; Moon, S. H.; Vannice, M. A. *J. Catal.* **1981**, *71*, 167.
(8) Liu, X. Y.; Liu, M. H.; Luo, Y. C.; Mou, C. Y.; Lin, S. D.; Cheng, H. K.; Chen, J. M.; Lee, J. F.; Lin, T. S. *J. Am. Chem. Soc.* **2012**, *134*, 10251.
(9) Yoon, K.; Yang, Y.; Lu, P.; Wan, D. H.; Peng, H. C.; Masias, K. S.; Fanson, P. T.; Campbell, C. T.; Xia, Y. N. *Angew. Chem., Int. Ed.* **2012**, *51*, 9543.
(10) Jia, A. P.; Jiang, S. Y.; Lu, J. Q.; Luo, M. F. *J. Phys. Chem. C* **2010**, *114*, 21605.
(11) Widmann, D.; Behm, R. J. *Angew. Chem., Int. Ed.* **2011**, *50*, 10241.
(12) Baker, L. R.; Kennedy, G.; Van Spronsen, M.; Hervier, A.; Cai, X. J.; Chen, S. Y.; Wang, L. W.; Somorjai, G. A. *J. Am. Chem. Soc.* **2012**, *134*, 14208.
(13) Yamada, Y.; Tsung, C. K.; Huang, W.; Huo, Z. Y.; Habas, S. E.; Soejima, T.; Aliaga, C. E.; Somorjai, G. A.; Yang, P. D. *Nat. Chem.* **2011**, *3*, 372.
(14) Somorjai, G. A.; Beaumont, S. K.; Alayoglu, S. *Angew. Chem., Int. Ed.* **2011**, *50*, 10116.
(15) Kleitz, F.; Choi, S. H.; Ryoo, R. *Chem. Commun.* **2003**, 2136.
(16) Taguchi, A.; Schüth, F. *Microporous Mesoporous Mater.* **2005**, *77*, 1.
(17) Lu, A. H.; Schüth, F. *Adv. Mater.* **2006**, *18*, 1793.
(18) Ren, Y.; Ma, Z.; Qian, L. P.; Dai, S.; He, H. Y.; Bruce, P. G. *Catal. Lett.* **2009**, *131*, 146.
(19) Rioux, R. M.; Song, H.; Hoefelmeyer, J. D.; Yang, P.; Somorjai, G. A. *J. Phys. Chem. B* **2005**, *109*, 2192.
(20) Pushkarev, V. V.; An, K. J.; Alayoglu, S.; Beaumont, S. K.; Somorjai, G. A. *J. Catal.* **2012**, *292*, 64.
(21) Zheng, F.; Alayoglu, S.; Guo, J. H.; Pushkarev, V.; Li, Y. M.; Glans, P. A.; Chen, J. L.; Somorjai, G. *Nano Lett.* **2011**, *11*, 847.
(22) Grass, M. E.; Karlsson, P. G.; Aksoy, F.; Lundqvist, M.; Wannberg, B.; Mun, B. S.; Hussain, Z.; Liu, Z. *Rev. Sci. Instrum.* **2010**, *81*, No. 053106.
(23) Yue, W. B.; Zhou, W. Z. *Prog. Nat. Sci.* **2008**, *18*, 1329.
(24) Sun, X. H.; Shi, Y. F.; Zhang, P.; Zheng, C. M.; Zheng, X. Y.; Zhang, F.; Zhang, Y. C.; Guan, N. J.; Zhao, D. Y.; Stucky, G. D. *J. Am. Chem. Soc.* **2011**, *133*, 14542.
(25) Rao, Y. X.; Antonelli, D. M. *J. Mater. Chem.* **2009**, *19*, 1937.
(26) Liang, Y. Y.; Li, Y. G.; Wang, H. L.; Zhou, J. G.; Wang, J.; Regier, T.; Dai, H. J. *Nat. Mater.* **2011**, *10*, 780.
(27) Tüysüz, H.; Schüth, F. *Adv. Catal.* **2012**, *55*, 127.
(28) Jia, C. J.; Schwickardi, M.; Weidenthaler, C.; Schmidt, W.; Korhonen, S.; Weckhuysen, B. M.; Schüth, F. *J. Am. Chem. Soc.* **2011**, *133*, 11279.
(29) Jansson, J.; Palmqvist, A. E. C.; Fridell, E.; Skoglundh, M.; Osterlund, L.; Thormahlen, P.; Langer, V. *J. Catal.* **2002**, *211*, 387.
(30) Thormahlen, P.; Skoglundh, M.; Fridell, E.; Andersson, B. *J. Catal.* **1999**, *188*, 300.
(31) Jansson, J.; Skoglundh, M.; Fridell, E.; Thormahlen, P. *Top. Catal.* **2001**, *16*, 385.
(32) McClure, S. M.; Lundwall, M.; Zhou, Z.; Yang, F.; Goodman, D. W. *Catal. Lett.* **2009**, *133*, 298.
(33) Cant, N. W.; Hicks, P. C.; Lennon, B. S. *J. Catal.* **1978**, *54*, 372.
(34) Berlowitz, P. J.; Peden, C. H. F.; Goodman, D. W. *J. Phys. Chem.* **1988**, *92*, 5213.
(35) Allian, A. D.; Takanabe, K.; Fujdala, K. L.; Hao, X.; Truex, T. J.; Cai, J.; Buda, C.; Neurock, M.; Iglesia, E. *J. Am. Chem. Soc.* **2011**, *133*, 4498.
(36) Doornkamp, C.; Ponec, V. *J. Mol. Catal. A: Chem.* **2000**, *162*, 19.
(37) Mars, P.; van Krevelen, D. W. *Chem. Eng. Sci., Spec. Suppl.* **1954**, *3*, 41.
(38) Mars, P.; Maessen, J. G. H. In *Proceedings of the Third ICC, Amsterdam*; North-Holland: Amsterdam, 1964; Vol. *1*, p 266.
(39) McCrea, K. R.; Parker, J. S.; Somorjai, G. A. *J. Phys. Chem. B* **2002**, *106*, 10854.
(40) Li, Q. F.; He, R. H.; Gao, J. A.; Jensen, J. O.; Bjerrum, N. J. *J. Electrochem. Soc.* **2003**, *150*, A1599.
(41) Weisz, P. B. *Adv. Catal.* **1962**, *13*, 137.
(42) Coonradt, H. L.; Garwood, W. E. *Ind. Eng. Chem. Process Des. Dev.* **1964**, *3*, 38.
(43) Alayoglu, S.; Krier, J. M.; Michalak, W. D.; Zhu, Z. W.; Gross, E.; Somorjai, G. A. *ACS Catal* **2012**, *2*, 2250.
(44) Bunluesin, T.; Gorte, R. J.; Graham, G. W. *Appl. Catal., B* **1998**, *15*, 107.
(45) Oku, M.; Hirokawa, K.; Ikeda, S. *J. Electron Spectrosc. Relat. Phenom.* **1975**, *7*, 465.
(46) Stranick, M. A. *Surf. Sci. Spectra* **1999**, *6*, 31.
(47) Oku, M.; Sato, Y. *Appl. Surf. Sci.* **1992**, *55*, 37.
(48) Xie, X. W.; Li, Y.; Liu, Z. Q.; Haruta, M.; Shen, W. J. *Nature* **2009**, *458*, 746.
(49) Park, J. Y.; Renzas, J. R.; Hsu, B. B.; Somorjai, G. A. *J. Phys. Chem. C* **2007**, *111*, 15331.
(50) Baker, L. R.; Hervier, A.; Seo, H.; Kennedy, G.; Komvopoulos, K.; Somorjai, G. A. *J. Phys. Chem. C* **2011**, *115*, 16006.
(51) Hervier, A.; Renzas, J. R.; Park, J. Y.; Somorjai, G. A. *Nano Lett.* **2009**, *9*, 3930.
(52) Maximoff, S. N.; Head-Gordon, M. P. *Proc. Natl. Acad. Sci. U.S.A.* **2009**, *106*, 11460.